Journal Pre-proof

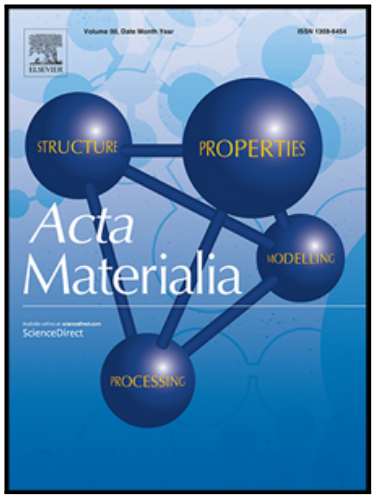

Tantalum and Zirconium induced structural transitions at complex [111] tilt grain boundaries in Copper

T. Meiners, J.M. Duarte, G. Richter, G. Dehm, C.H. Liebscher

PII: S1359-6454(20)30178-6
DOI: https://doi.org/10.1016/j.actamat.2020.02.064
Reference: AM 15888

To appear in: *Acta Materialia*

Received date: 4 October 2019
Revised date: 27 February 2020
Accepted date: 28 February 2020

Please cite this article as: T. Meiners, J.M. Duarte, G. Richter, G. Dehm, C.H. Liebscher, Tantalum and Zirconium induced structural transitions at complex [111] tilt grain boundaries in Copper, *Acta Materialia* (2020), doi: https://doi.org/10.1016/j.actamat.2020.02.064

Effect of Zr on the structure of copper grain boundaries

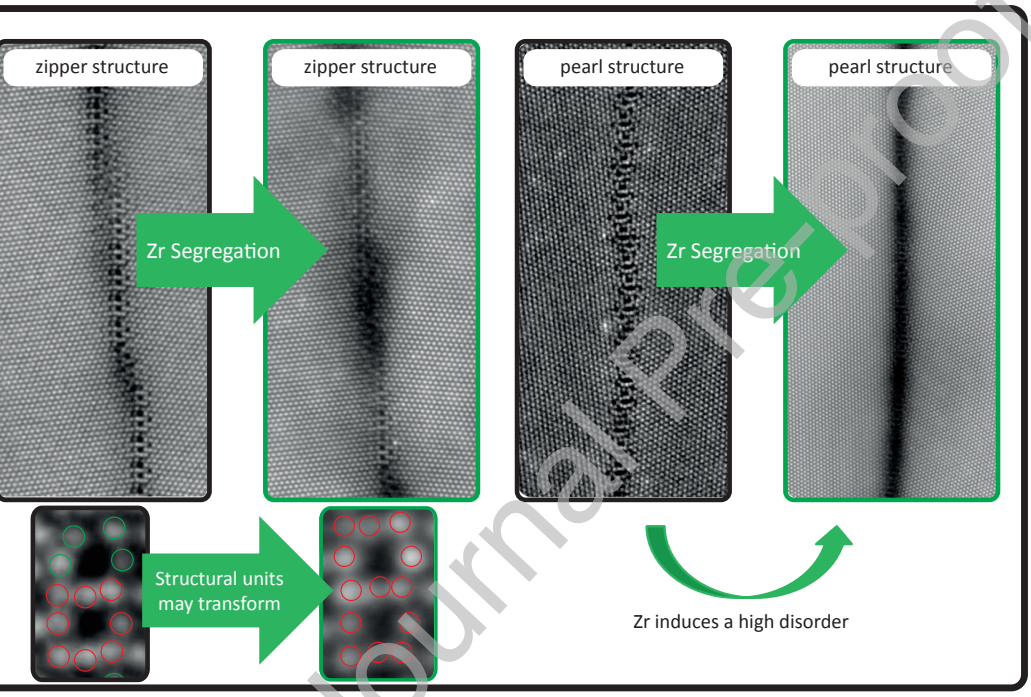

GB pinning in Cu by Ta particles

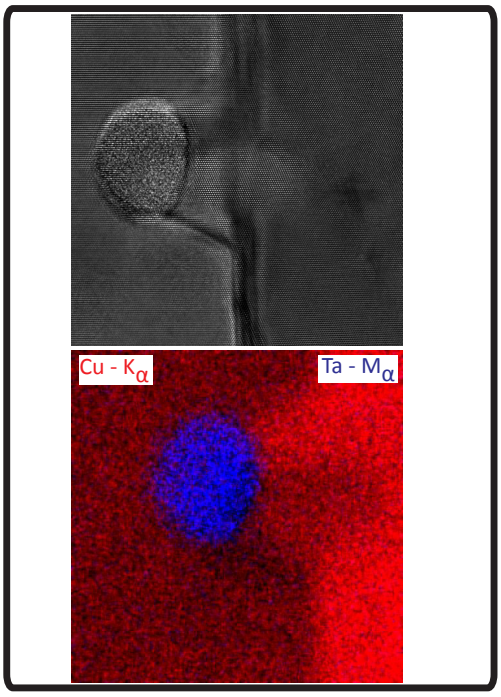

Tantalum and Zirconium induced structural transitions at complex [111] tilt grain boundaries in Copper

T. Meiners[a], J.M. Duarte[a], G. Richter[b], G. Dehm[a], C.H.Liebscher[a,]

[a] *Max-Planck-Institute for Iron Research GmbH*
[b] *Max-Planck-Institute for Intelligent Systems*

Abstract

Alloying nanocrystalline copper with immiscible elements, such as tantalum (Ta) and zirconium (Zr), is a promising technique to manipulate grain boundary properties and by this suppress grain growth at elevated temperatures. However, insights on the atomistic origins on the influence of impurity elements on grain boundaries are lacking. In this study, the atomistic effects of Ta and Zr on [111] tilt grain boundaries in Cu are investigated by high resolution scanning transmission electron microscopy techniques. In case of Ta, the formation of spherical, nano-scale precipitates in close vicinity to the grain boundaries is observed, but no sign of segregation. The particles induce a repelling force to migrating boundaries and act as local pinning points. The segregation of Zr is observed to occur either at confined grain boundary steps or homogeneously along the boundaries without steps. In both cases as strong disordering of the defect or grain boundary structure is revealed. Furthermore, at low Zr concentrations it induces structural GB transitions and partial atomic reordering of the grain boundary structural units.

Keywords: Grain boundaries, atomic structure, transmission electron microscopy, structural transitions, grain boundary pinning

1. Introduction

Grain boundaries (GBs) have been investigated over many decades because of their enormous importance to tailor material properties [1, 2, 3, 4, 5]. Even

though many experimental and theoretical studies have been employed to unravel the structure, energy, mobility and diffusion behavior of special GBs, a detailed understanding of the atomistic mechanisms of GB segregation effects and their impact on GB properties is lacking [6, 1, 7, 8, 9, 10, 11, 4]. The main challenge to establish a generalized picture in this field results from the huge variety of GB types [2], the difficulty to experimentally access their atomic structure and to correlate it directly to the GB properties. Mostly atomistic simulations are employed to explore GB structures and effects of impurity segregation, although these studies are limited by the accessibility of reliable semi-empirical atomic potentials [1, 12, 13, 14, 15].

Already $\sim$ 50 years ago the structural unit (SU) model was introduced in order to describe the atomic structure of special coincident site lattice (CSL) GBs by repeating 2D building blocks [16, 1, 12]. A GB that consists only of one single unit type is called a delimiting boundary. The SU model predicts that each GB with misorientation Θ can be constructed using only the units from the delimiting GBs. Many theoretical studies focused on the description of the structural units of different symmetric and asymmetric GBs [6, 7, 1, 12]. Frost et al. [6] presented a catalogue of predicted structures for [001], [011] and [111] symmetric tilt GB in face-centered cubic (fcc) hard sphere crystals. Wang et al. [7] followed the approach and presented structures of [001] and [111] tilt GBs and their energies. However, more recent studies have shown that the SU model does not work in general for all kinds of GB, e.g in low stacking fault materials and for long period GBs [17, 18]. Therefore, the SU model was revisited and extended by Han et al. [19] including stable and metastable GB structures as delimiting boundaries.

The development of aberration-corrected transmission electron microscopes (TEM) made possible to experimentally access the atomic structure and chemistry of GBs. In recent years, several studies explored the atomic arrangements of special tilt GBs in ceramic, metallic and semiconductor systems [20, 21, 22, 23, 24, 9, 25]. Yu et al. also showed that periodic segregation pattern can be formed at more general GBs and that these reconstruction are not dependent

on the grain misorientation but rather on the orientation of the terminating grain surfaces [25]. In combination with complementing atomistic simulations it is possible to unravel intrinsic GB properties, such as segregation behavior or cohesive properties. These detailed insights enabled GB engineering as a major research field in order to tailor materials properties by manipulating the structure and chemistry of GBs [26]. Introducing impurity elements at GBs is a promising way to modify specific GB properties, such as cohesion, mobility and energy. The reason for such property deviations can be explained by structural and chemical transitions, which are difficult to access at atomic resolution due to experimental restrictions [27, 28, 29, 10]. Recently, Peter et al. reported on segregation-induced nano-faceting transition of an asymmetric copper (Cu) tilt GB [24]. Only the combination of atomic resolution scanning TEM (STEM) and molecular dynamics simulations were able to reveal the underlying atomistic and thermodynamic origins for the nanofacet formation.

An emerging field where GBs and their transitions play an important role are nanocrystalline (nc) and nano-structured materials [30, 31, 32, 33, 34, 35]. They have recently received broad attention because of their unique properties. Especially the mechanical behavior of such materials is to mention here since the yield and flow stress as well as the hardness can increase quite significantly [36, 37, 38, 39]. Nanocrystalline Cu is a particularly interesting candidate because of the excellent electrical and thermal conductivity of Cu [5] and its remarkably high strength [40, 36]. However, rapid grain growth and the resulting instability of the microstructure at elevated temperatures strongly limit its commercial application. A way to stabilize the grain structure up to the melting point has been achieved by alloying with immiscible elements. It has been proposed that these elements tend to segregate to GBs and either kinetically or thermodynamically prevent grain growth. The kinetic approach utilizes second phase precipitation to pin migrating GBs, a process know as Zener pinning [41, 42]. In the thermodynamic approach, the GB free energy is reduced by solute segregation and thus the driving force for grain growth is decreased [43, 44, 45]. Two prominent candidates for stabilizing the nc grain structure are

zirconium (Zr) and tantalum (Ta).

The formation of nano-scale Ta clusters or precipitates in nc Cu have been shown to increase the strength and stability of the microstructure, referred to as kinetic approach. In ref. [46] the hardness was found to increase by more than a factor of 2 compared to pure Cu with comparable grain size. Close to the melting temperature the alloy suffered less from grain growth and could retain the extreme hardness. At the same time, the Cu matrix maintains its excellent electrical and thermal properties [47, 48]. However, a major disadvantage is the production of these alloys. Not only the solubility of Ta in Cu is neglegible [49], but also the diffusion of Ta inside the Cu matrix is at temperatures below $1000° C$ [46]. Furthermore, the underlying atomistic mechanisms of Ta segregation to GBs and GB pinning have been explored mainly by simulations. Only a few detailed TEM studies exist, investigating the effect of Ta on the atomistic mechanisms of GBs, e.g ref. [50, 46].

Zirconium was seen as an excellent candidate to stabilize nc Cu due to its poor solubility in Cu ($0.12\,at.\,\%$ at $972° C$ [51]), the tendency to segregate to GBs and glass phase formation [52]. Atwater et al.[53] showed that adding only $1\,at.\%$ Zr can stabilize the nanoscale grain size by forming small scale intermetallic phases and Zirconia (ZrO_2) at GBs. In contrast, Khalajhedayati et al. [52] reported the formation of amorphous intergranular films, which are assumed to reduce the GB energy and therefore the driving force for GB migration.

In this study, the effect of Ta and Zr on the atomic structure is investigated. In order to observe the atomic structure of GBs in TEM, both grains need to share a common zone axis parallel to the electron beam direction, which is true for tilt grain boundaries. Textured thin films with mainly [111] tilt GBs This can be achieved by growing Cu thin films growth onto sapphire (0001) substrates, which and is explained in detail in Ref. [54]. Thus, defined [111] tilt GBs are produced by molecular beam epitaxy (MBE) in order to systematically study the same GB structures and possible structural transitions by the addition of solute atoms (Ta and Zr). The representative GBs in this work are two symmetric $\Sigma\,19\,b$ and corresponding asymmetric variants, with deviations of maximum

$\sim 6°$ from the symmetric orientation. The $\Sigma 19\,b$ is amongst the most common special and low Σ GB in these films and can be easily reproduced. It was found that they occur in two symmetric variants and vicinal asymmetric GBs. The GBs exhibit long period structural units, which can be further decomposed into sub-units. Even though only the GB inclination changed by $30°$, the two GBs show strongly differing atomic structures, which do not agree with the SU model as described above. The Cu films are alloyed by sputter depositing Ta and Zr thin films at room temperature followed by a subsequent post-deposition annealing treatment and it is shown that GB diffusion is fast enough to introduce large amounts of Ta and Zr into the GBs. The effect of both impurity elements on the atomic structure is investigated by aberration-correct STEM. It is shown that this is a simple process to introduce spherical, nano-scale Ta precipitates at GBs, which act as local GB pinning points by bending the local GB plane. The segregation behavior of Zr is observed to occur in two different ways. At a planar asymmetric GB, Zr homogeneously decorates the GB and causes a strong disordering of its atomic structure. Confined Zr segregation to GB steps is observed for a nano-faceted GB, where the steps are more disordered compared to the clean GB steps. At the symmetric GB facets structural transitions compared to the clean GB facets are observed.

2. Experimental Details

Cu thin films were grown by molecular beam epitaxy at room temperature on (0001) oriented Sapphire substrates followed by a post-deposition annealing for 4 hours at $400\,°C$. For the segregation experiments, the Cu film surface was sputter cleaned prior to deposition of Ta and Zr thin films. Subsequently, $50\,nm$ Ta and $100\,nm$ Zr films were deposited each separately at room temperature on a small piece of the Cu film. The Zr/Cu film was annealed for ~ 5 hours at $\sim 400\,°C$ under high vacuum conditions. The annealing temperature and time were chosen rather small in order to prevent the formation of intermetallic phases at the GB and the sample surface. The Ta/Cu film, however, was an-

nealed for ~ 24 hours at $\sim 600\,^{\circ}C$. Since Ta diffusion in Cu is almost zero, a much higher temperature and longer annealing time was chosen in order to activate GB diffusion. A higher temperature for higher diffusion was not chosen to be sure that the films remain thermally stable and prevent dewetting of the Cu film. Therefore, the temperature was chosen to be at least half of the absolute melting temperature of Cu. Thin film texture and global grain structure was determined by electron backscatter diffraction (EBSD) in a JSM-6490 (JEOL) operated at an acceleration voltage of $30\,kV$. TEM specimens of special GBs were prepared either by a site-specific plan-view focused ion beam (FIB) lift-out as described in ref. [55, 56] or as conventional cross-section lift-outs using a dual beam SEM / FIB instrument Helios Nanolab 600i (Thermo Fischer Scientific). EBSD has been performed only on the pure Cu films, since no diffraction pattern could be recorded through the remaining Ta and Zr. STEM imaging was performed in a probe-corrected FEI Titan Themis $60-300$ (Thermo Fischer Scientific) S/TEM equipped with a high-brightness field emission gun and gun monochromator operated at an accelaration voltage of $300\,keV$ using a high angle annular dark field (HAADF) detector (Model 3000, Fischione Instruments). The semi-convergence angle was chosen to $17\,mrad$ and HAADF images were recorded with a collection angle range of $73-200\,mrad$ and a probe current of $\sim 80\,pA$. For energy-dispersive X-ray spectroscopy (EDS) the probe current was raised to $\sim 150\,pA$ and X-rays were collected with the ChemiSTEM system (Thermo Fisher Scientific). Bright field (BF), dark field (DF) and high resolution TEM imaging was done in an image-corrected FEI Titan Themis $80-300$ (Thermo Fischer Scientific) TEM under negative C_s $(-10\,\mu m)$ conditions using an accelerating voltage of $300\,keV$ [57].APT specimens were prepared by site-specific FIB lift-out using a dual beam workstation Helios Nanolab 600i from Thermo Fischer Scientific. Final low energy cleaning at 5 kV and 40 pA was performed to minimize the Ga content in the sample, which was found to be at the background level in the regions of interest. The measurements were conducted in a LEAP 5000 XR local electrode APT from Cameca Instruments in laser pulsing mode. The specimen temperature was set to $50\,K$, while the

laser pulse energy of $85\,pJ$ at a frequency of $125\,kHz$ were used to evaporate the sample at a detection rate of 0.7 %. The presence of oxides and other impurity elements was detected only close to the top surface indicating possible contamination during sample preparation and transfer between instruments. These initial sections, corresponding also to the Zr film, were discarded to focus on the Cu grains and their GBs and no further oxides were found.

3. Results

3.1. Global thin film grain boundary structure

EBSD reveals that the Cu films grow with [111] texture, as shown by the inverse pole figure (IPF) map in Fig. 1. The film's grain structure is shown in the image quality map (IQM). The grain size can be determined to $\sim 100\,\mu m \pm 50\mu m$. The large error in average grain size results from a strong scatter in the grain size distribution, which includes grains with diameters of $\sim 300\,\mu m$ down to $\sim 10\,\mu m$. The grain size distribution is shown in Fig. 1 (c). Most grains exhibit a round shape (in 3D it is therefore cylindrical due to small film thickness compared to the grain size), which translates to continuous changes in GB inclination along each grain boundary. Approximately 80% of the GBs are low angle and twin boundaries ($\Sigma 3$). The remaining ones are different low Σ boundaries, such as $\Sigma 7$ (~ 1 %), $\Sigma 9$ (~ 0.3 %), $\Sigma 19b$ (~ 7 %), $\Sigma 31a$ (~ 2.5 %), $\Sigma 37c$ (~ 8 %). The most frequent GBs are highlighted by colored lines in Fig. 1. The white/black regions in the center of the IPF/IQM illustrates positions from where TEM specimens were extracted by FIB. This procedure ensures that each TEM specimen only contains specific, pre-selected types of CSL boundaries; in the present case a $\Sigma 19b$ GB.

3.2. Atomic structure of pure $\Sigma 19$ *brain boundaries*

The atomic structure of four different GBs is depicted in Fig. 2 and Fig. 3. Two are symmetric $\Sigma 19b$ with a misorientation of $\sim 47°$ and GB habit planes $(2\bar{5}3)$ and $(1\bar{8}7)$, which corresponds to a change in boundary plane inclination

of 30° (see Fig. 2 (a) and (c)). The other two GBs are asymmetric variants of the two symmetric GBs with different GB plane orientation resulting in small angular deviation between $\sim 2-6°$ (Fig. 3 (a) and (d)).

The $\Sigma 19\,b\,(2\bar{5}3)$ in Fig. 2 (a) is a straight and flat GB, which remains in the symmetric orientation for $\sim 100\,nm$. It is difficult to observe longer segments of these GB orientations, since the grains have mostly a cylindrical shape and therefore the GBs are often stepped or faceted. In between these segments, the same symmetric structural units can be consistently observed. The common description of CSL GB structures is obtained by characteristic structural units (SU) [16, 19]. The full SU of the $\Sigma 19\,b\,(2\bar{5}3)$ can be divided into two sub-units as highlighted by red and green circles in the magnified view of the yellow rectangle of Fig. 2 (b). The filled red circle marks the CSL positions at this GB. The red sub-unit exhibits a square shape formed by 8 atomic columns followed by the green sub-unit, a trapezoid consisting of 4 columns. According to the nomenclature of the SU model, the GB structure can be written as $|\ ST\cdot ST\ |$, where S represents the red, squared and T the green, trapezoidal sub-unit. According to [19], the vertical lines | represent one GB period along the GB plane and " $\cdot$ " means that the sub-units are shifted along the GB by a half period. In the whole GB segment these two sub-units alternate and form the GB and disruptions of this sequence at the symmetric segments were not observed. With respect to its appearance, this GB structure is termed zipper structure in the following.

The $\Sigma 19\,b$, $(1\bar{8}7)$ shows a very different atomic structure (see Fig. 2 (c)) with a change in GB inclination by 30° . This boundary also remains straight over a length of $\sim 100\,nm$, but its SU appear completely different to that of the zipper structure. The red box highlights the region of the GB from where the SU are displayed in magnified view in Fig. 2 (d). Also here, two characteristic sub-units, marked by green and red circles, are observed. A particular arrangement of four of these sub-units builds up the repetitive unit of the GB. The green sub-unit consists of one "pearl chain" type arrangement (5 atomic columns) and one distorted rectangle (red), similar to the red sub-unit of the zipper structure.

The total SU is composed of a combination of these two sub-units, which are mirrored with respect to the grain boundary plane, as is indicated in Fig. 2 (d) by the SU model notation. Here the SU notation is $\mid RP \cdot Я\,Ꟁ \cdot RP \cdot Я\,Ꟁ \mid$, where R represent the distorted rectangle (red), P the pearl chain (green) and the Я and Ꟁ the mirror operation of the two sub-units with respect to the GB plane. It is obvious that this GB exhibits a longer period structure, since 4 sub-units build up a full SU. Also here, no deviation from this arrangement was observed for the symmetric boundaries. The filled red circles show CSL positions switching periodically from the left to right side of the GB due to the mirror operation of the sub-units. This GB structure is termed pearl structure in the following.

Asymmetric GBs with a small deviation of $\sim 2-6°$ from the symmetric orientation are frequently observed for both $\Sigma 19b$ boundaries when tracing the GBs. For each GB one example is illustrated in Fig. 3 (a) and (c). Interestingly, both GBs show a different way of compensating for the asymmetric inclination of the GB habit plane. In case of the zipper structure, the GB dissociates into $\sim 4\,nm$ long symmetric $(2\bar{5}3)$ facets that are regularly interrupted by steps as illustrated in Fig. 3 (a) and (b)). The magnified view, indicated by the purple rectangle, in Fig. 3 (b) highlights a GB step and shows an extended, disordered core structure. The CSL of the single symmetric facets still fit nicely together (not shown here) so that the step seems to be a shift along the CSL. The facet length, and hence the number of steps, as well as the step height of $\sim 0.5\,nm$ adjusts in such a way as to compensate for the overall deviation in grain boundary plane inclination from the symmetric orientation of $\sim 5°$. For the pearl structure, a different scenario is observed, as demonstrated in Fig. 3 (c). Instead of decomposing into facets and steps, here, the asymmetric GB plane remains straight and incorporates additional sub-units to compensate for the asymmetric inclination, as indicated by blue arrows (Fig. 3 (d)). The inset (see Fig. 3 (c)) shows a magnified view of the area highlighted by the blue rectangle. These sub-units appear similar to the "pearl chain" (green sub-unit) of the symmetric case and their repeat distance depends on the magnitude of

angular deviation. In the present GB, this deviation is $\sim 3°$ and the repeat distance of the extra units is $\sim 2\,nm$.

3.3. Tantalum segregation and grain boundary pinning

Fig. 4 shows conventional and high resolution TEM images of a cross-section specimen of the Cu film alloyed with Ta. The alumina substrate is located at the bottom, the Cu thin film containing a GB in the central region and the $50\,nm$ Ta film is located in the top part of the BF TEM image of Fig. 4 (a). The length of the GB was measured to $\sim 975\,nm$ and its overall appearance is straight. However, the region highlighted by a blue box, reveals a step towards the right grain, as shown in the HRTEM image in Fig. 4 (b). The step size is measured to $\sim 6.4\,nm$. Along the GB three of these steps can be observed, as illustrated by the blue arrows in Fig. 4 (a) so that the total step height between the top and bottom part of the GB adds to $\sim 18\,nm$. Therefore, it can be assumed that the GB migrated towards the right during heat treatment. Furthermore, a spherical Ta precipitate with $\sim 14.4\,nm$ in diameter is observed roughly in the middle part of the GB, directly in front of the step (see Fig. 4 (b)). A particle found in the upper GB region (red box) is illustrated in the BF image of Fig. 4 (c). It shows a more elliptical shape with a size of $\sim 12.4\,nm$ and $9.1\,nm$ and is directly located besides the GB, while the image contrast reveals that it is still connected to the GB. The high resolution TEM image of Fig. 4 (d) shows that the right grain is in [011] zone axis orientation, while the left grain is off zone axis and only the $(\bar{2}00)$ lattice planes can be resolved. We observe that the grain boundary still adheres to the particle and that the right grain in front of the particle is extended into the region of the left grain, twisting the GB plane. It appears that the GB moved across the precipitate, but was not able to detach from its backside. A STEM-EDS measurement in the same region and magnification as Fig. 4 (d) identifies the particle as a Ta precipitate. An elemental map of the Cu-$K\alpha$ and Ta-$L\alpha$ map is shown in Fig. 5 (a) and the corresponding X-ray spectra, one from the Cu matrix (red) and one from the particle (blue), in Fig. 5 (b). Additionally, a pronounced oxygen

peak is observed in the region of the Ta-particle indicating that the particle could be oxidized. However, it should be mentioned that this might also be a result of the FIB sample preparation process and more likely, exposure of the specimen to air during sample handling. From the high resolution image in Fig. 4 (d), the particle appears amorphous. Investigating the fast Fourier transform (FFT) of HRTEM images in other orientations and different particles did also not reveal any indication that the particles are crystalline. An example of an FFT obtained only from the Ta-particle is shown in the inset of Fig. 4 (d).

3.4. Zirconium segregation and grain boundary disordering

Adding Zr to the thin film reveals a different segregation behavior than for Ta. The results for an asymmetric $\sim 49°$ [111], $(16\bar{5})\backslash(1\,\bar{1}\,\bar{6}\,15)$ GB with the pearl structure is shown in Fig. 6 (a). The planes deviate from the symmetric $(1\bar{8}7)$ plane by $\sim 2.3°$ and $\sim 3.4°$. In the STEM micrograph, the GB appears dark under HAADF conditions and the identification of structural motifs is barely possible. This contrast is observed almost entirely along the GB. A magnified view of the atomic structure is illustrated in the insets of regions highlighted by purple and red rectangles in Fig. 6 (a). A strong high pass Fourier filter was applied in order to emphasize the structure. Despite the weak atomic column contrast, similar structural units, indicated by green and red dots, as in the pure Cu GB of Fig. 3 (d) can be identified in the purple region. But as shown in the area marked by a red box in Fig. 6 (a), distorted or even disordered variants of the structural motifs are observed. The blue colored atomic columns show additional sub-units resulting from the asymmetry of the GB. In the upper region only one line of extra atomic columns is visible, while two extra lines are found in the lower part. The STEM-EDS maps of the Cu-L_α and Zr-L_α X-ray lines taken in the purple region of Fig. 6 (a) are illustrated in Fig. 6 (b) and clearly reveal that the GB is strongly decorated with Zr. The corresponding X-ray spectra, taken from the grain interior (red) and at the GB (green) are shown in Fig. 6 (c). The inset in the spectrum, indicated by a dashed box, illustrates the intensity modulation of Cu, Zr and O by taking a line scan across the GB.

The maximum standard deviation of the EDS line profiles was determined by calculating the standard deviation in a sliding window of $\sim 0.5\,nm$ and is shown as inset in Fig. 6 (c). The peak-to-noise ratio of the integrated Zr-L_α X-ray line profile across the GB is ~ 4 indicating clear evidence for Zr enrichment. No clear sign of O enrichment at the GB is observed in the line scan, although a slight oxygen (O) peak is present in the GB spectrum of Fig. 6 (c)). All together, Zr leads to a strong disordering of the GB structure, which leads to displacements of atomic column positions perpendicular to the viewing direction. This in turn, leads to de-channeling of the electrons, which leads to an effective reduction of the atomic column intensity in the HAADF images.

In the case of an asymmetric $\sim 49°$ $[111], (12\bar{3})\backslash(\bar{2}11)$ GB, adapting the zipper structure, an inhomogeneous segregation of Zr is observed, which appears as dark contrast regions at the GB steps as seen in the HAADF image of Fig. 7 (a) (marked by the white arrows). The corresponding STEM-EDS measurements reveal that these regions are Zr and O rich, as can be seen from the corresponding X-ray spectrum extracted from the orange rectangle in Fig. 7 (b). The Zr signal disappears almost entirely at the symmetric GB facets (blue rectangle) and within the Cu matrix (magenta rectangle). This observation is further supported by two intensity profiles extracted across the GB and the GB step, as indicated by arrows. A drop in Cu signal at the GB step is observed, while both Zr and O intensities increase (Fig. 5c). In this line profile the O and Zr signal are more noisy compared to the former example in Fig. 6 (c), again illustrated by the maximum standard deviation shown in the insets in Fig. 7 (c) and (d). In the case of the GB step, the peak-to-noise ratio of the integrated Zr-L_α X-ray line profile is only ~ 2, which is high enough to confirm segregation of Zr to the GB steps. The O intensity increase may be a result of oxidation of Zr in the GB step, but in view of the APT measurements on a fully Zr decorated GB shown in Fig. 9, a complete Zr-oxide formation is unlikely. The detection of O in each location of the specimen indicates that the surface of the TEM specimen was oxidized. The large Zr rich regions are mainly located at the steps between symmetric segments, but also smaller Zr rich regions in the

clean symmetric segments are observed rarely (seen also as black contrast), as illustrated in Fig. 8 (a) in the green rectangle. A $0.5\,nm$ wide dark spot can be seen in the middle of the clean symmetric facet, indicating that also here small amounts of Zr could be located in such confined regions. While the facets of the clean GB show a homogeneous length distribution, the facet length in the Zr segregated case varies between $1\,nm$ (first facet in Fig. 8 (a)) and $6\,nm$ (facet in the image center in the green box). This can either be induced by the Zr segregation or could also be due to the local GB curvature. Such a behavior was not observed for a clean GB, but the statistics on these observations are low. Furthermore, the steps differ in contrast with respect to each other, suggesting that the amount of Zr differs for each step.

Since the quantification of STEM-EDS data obtained under strong channeling conditions used here is limited, more precise information on the GB composition was obtained by APT shown in Fig. 9. As EBSD measurements were not successful, because of the remaining Zr film on top of the Cu, it is not known what kind of GB was investigated here. But it still gives very good and detailed information about the elemental distribution and the amount of Zr segregated to the GBs. To directly relate the GB structure and the chemistry, one would need to do correlative TEM and APT measurements. The reconstruction in Fig. 9 (a) shows all Cu atoms as red and Zr atoms as green dots. Zr is segregated homogeneously along this GB and its accumulation can be better approximated in the concentration profile (see Fig. 9 (c)). In the corresponding mass spectrum, no significant amount of oxygen was found within the detection limit. It is concluded that pure Zr is located at the GB core and no intermetallic Cu-Zr phases or a Zr_xO_{1-x} were formed, as intended by the annealing treatment. The solute atomic excess of Zr at the GB was calculated following ref [58, 59] with an average of $2.76 \pm 0.24\,\frac{at}{nm^2}$. The absence of oxygen signal in the APT data supports that variations in the oxygen signal of the STEM-EDS data are mainly related to surface oxidation.

Looking deeper into the atomic structure of the symmetric, Zr free appearing facets, an influence of Zr on the structural sub-units can be observed. Such

regions are marked by a green and orange rectangle (facet and step region) and its magnified views are illustrated as an inset in Fig. 8 (a)). The atomic structure of the Zr decorated steps (orange box) is strongly disordered (compared to the clean step from Fig. 3 (b)), which also explains the decrease in contrast despite the segregation of an atomic species with higher atomic number than Cu. In certain locations, the SU observed at clean symmetric and asymmetric GBs (Fig. 2 (a) and Fig. 3 (a)) appear to undergo slight structural transitions upon Zr segregation. Locations where these structural modifications are indicated by yellow rectangles in the insets of Fig. 8 (a). In contrast to the original SUs, the modified units are only composed of rectangular building blocks (red sub-units) leading to a disruption of the periodicity of GB structural units. In Fig. 8 (b), the structure of the clean symmetric and asymmetric GB are compared with the Zr influenced symmetric facet. The blue and yellow boxes show the SU of the clean and Zr induced GBs. On the bottom of Fig. 8 (b) the structural transition is visualized. The transformation can be described by adding one atomic columns to the green, trapezoidal SU, which transforms it into the red, rectangular SU. This seems to occur without any periodicity/ ordering along the GB facets so that the overall periodicity and order is decreased.

4. Discussion

In the first part of this discussion the complexity of the two $\Sigma 19b$ GBs, investigated here, will be discussed with respect to the SU model. To the authors knowledge, there are no other experimental studies on the atomic structure of [111] tilt GBs in fcc metals, but only theoretical calculations, for example from Frost et al. and Wang et al. [6, 7] . Afterwards, the influence of Ta and Zr on the atomic SU of the GBs is discussed in detail. Furthermore, the results are compared with recent studies on similar material systems and conclusions on how this is related to the microstructure stabilization of nanocrystalline Cu are drawn.

4.1. Pure Σ19b[111] tilt GB structures

Both experimentally observed Σ19*b* GBs exhibit the same grain misorientation and only differ in habit orientation leading to a significant change in their structural sub-units. In total, 4 different structural sub-units, S,T,R and P, could be assigned to fully describe the structure of the grain boundaries. Originally it was proposed that each GB with a specific misorientation can be constructed by the structural units of two delimiting boundaries (with respect to misorientation) [16]. This model is not applicable to the present GBs even though we do not know the SU from the delimiting GBs. Since a delimiting boundary is supposed to consist of only one SU [19], according to the SU model there exist only two SU, e.g. one from the 0° and on from the 90° GB, in order to build up other GBs (as it is done for the Σ5[001]) [19]. But the two Σ19*b* GBs here already revealed 4 different SUs so that two delimiting boundaries would be not enough to describe both Σ19*b* simultaneously. Therefore, the extended model by Han et al. [19] could be considered, since it also takes meta stable GB structures as possible delimiting GBs into account and thus the number of available SUs is increased. But this is not investigated in that detail nowadays so that it cannot be discussed further. Deviations from the SU model have been also found by other theoretical studies in different symmetric tilt GBs [18, 17, 19].

[111] tilt GBs in fcc metals are much less studied than [001] or [011] tilt boundaries. To our knowledge, only two theoretical studies exit reporting on the structure of several of the [111] tilt GBs [6, 7]. Frost et al. estimated the structure and properties of different low Σ GBs by a simple hard sphere model [60]. Comparing their predicted structures to the ones observed in experiment here reveals a fundamental difference in the structural units of both Σ19*b* boundaries. This indicates that the hard sphere model is not capable of predicting the structure of [111] tilt GB. A similar conclusion is found by comparing the experimentally obtained structures here with the calculated ones of Wang et al. [7]. They describe the structure of the Σ19*b*$(2\bar{5}3)$ with the SU model notation $|\ EFF\cdot EFF\cdot EFF\ |$ by using the Σ1$(1\bar{1}0)$ and Σ3(121) as delimiting GBs.

E represents a special unit of the $\Sigma 1$ and F of the $\Sigma 3$ boundary. It is obvious that their notation/structure does not fit to the experimental observations in the present study $\mid ST \cdot ST \mid$ and $\mid RP \cdot Я\P \cdot RP \cdot Я\P \mid$.

4.2. Cu-Ta system

The formation of spherical, nanometer sized Ta-rich particles is only observed at or near GBs, leading to the conclusion that GB diffusion is the dominating process, while diffusion into the grains is not possible at this temperature. This is not surprising since Ta diffusion tends to zero in bulk Cu below $1000°C$ and the annealing treatment here was performed at $600°C$ [46]. Apparently, diffusion of Ta along the entire $\sim 1\,\mu m$ long Cu tilt GBs occurred during the heat treatment for $24\,h$ at $600°C$. Ta homogeneously distributes along the GBs during annealing, since the bulk solubility of Ta in Cu is essentially zero below $\sim 1038°C$ [49]. During cooling, the solubility of Ta at the GB decreases and excess Ta atoms accumulate to form spherical particles. In total, three steps are observed and the GB moved in total $\sim 18\,nm$, which would correspond to an average velocity of $2 \cdot 10^{-4}\,\frac{nm}{s}$ to the right side (considering a constant movement for $24\,h$). It can be assumed that while Ta homogeneously distributes along the GB it lowers its mobility at $600\,°C$ due to the solute drag effect [61]. During cooling, Ta precipitates out at the GB and the mobility of the Ta lean parts increases. It seems that the GB groove at the film surface acts as a step nucleation site first promoting the motion of the upper part of the GB. Subsequently, this part of the boundary starts migrating and sweeps across the Ta precipitates and gets pinned at its backside. The exerted backstress of the particle impedes GB migration. This pinning of GBs by particles was discussed in theoretical studies before and is known as Zener pinning [62]. The Zener model describes grain growth of a particle containing matrix, where the driving force for GB migration is counteracted by a pinning pressure between the surface of the particle and the GB plane [42, 41]. Depending on the direction of GB migration and the position of the particles, they can either exert an attractive or repelling force on the GB. It is proposed that the particles induce a local

curvature in the GB, which then leads to a driving force towards the particle. This is schematically depicted in fig. 10 (a), adapted from [42]. Applying this force balance to our experimental observations allows to estimate the fraction of local pinning force on the GB for a given particle radius r, even though the local surface tension γ between GB and particle is not known:

$$F_z = 2\pi\, r\gamma \sin(\theta)\cos(\theta) \tag{1}$$

In equation 1, θ defines the contact angle between the average surface of the GB plane and the point where it crosses the particle [41]. The force on the GB is at its maximum (attracting or repelling) for an angle of 45 °. In the experimental image, the GB does not follow a smooth curvature but appears discontinuous and deviates strongly from the exact model (see fig. 10 on the right the white line). This makes it difficult to precisely determine the correct contact angle. But here, two variants can be calculated and it can be assumed that the real value lies in between these two. First, the angle between the particle center and the kink (marked in red in the figure) can be measured to an angle of $\sim 45\,°$, which means that maximum force is pulling on the GB in the observed configuration. Secondly, one can measure from the particle center to the point of contact (marked in green) an angle of $\sim 25\,°$, which leads therefore to $\sim 77\%$ of the maximum force. Since the GB moved to the right side considering the GB steps from fig. 4(e), the particle is exerting a repelling pinning force on the GB at this moment. A single nano-sized particle is in principle not enough to pin a whole GB, but with a higher particle density the Zener model predicts a limited grain size.

The atomic resolution images clearly reveal the Zener effect of Ta particles at Cu GBs. The observations are in excellent agreement with theoretical studies [62, 63, 46, 64] and the proposed Zener model [42, 41]. Hence, the segregation of Ta to Cu GBs and the associated GB pinning by Ta particles can be associated to the kinetic approach for stabilizing microstructure.

4.3. Cu-Zr system

A recent study by Khalajhedayati et al. shows that adding Zr not only leads to a stabilization of the microstructure of nanocrystalline Cu-Zr alloys, but also increases the strength while conserving partly the ductility of polycrystalline Cu [52]. In their study, they presented that either amorphous intergranular films (AIFs) form at the GB or that Zr homogeneously decorates the GB, depending on the processing route of the material. They propose that the AIFs reduce the GB mobility and ductility is partly retained, while homogeneous Zr decoration only reduces GB mobility and leads to embrittlement. However, direct atomic scale correlation of the presence and effects of Zr on the GB structure (with EDS for example), also compared to clean GBs in their material, are missing in the study [52]. In a different publication, however, they presented some EDS analysis in lower magnification in similar samples and showed a slightly inhomogeneous Zr segregation and a Zr concentration as high as $\sim 7at.\,\%$ [65]. Another study of Pan et al. [66] deals with atomistic calculations of the Zr segregation behavior at different GBs considering several Zr concentrations and annealing temperatures. They found that AIF formation depends on the Zr concentration, the GB structure and annealing temperature. Low Zr concentration and low annealing temperature lead more to defined segregation and a crystalline GB structure, while increasing both leads to amorphization. The concentration and temperature for the transition also depends strongly on the GB structure. In the present study, considering the two different $\Sigma\,19b$ variants observed, three different phenomena can be observed:

1. The $\Sigma\,19b\,(1\bar{8}7)$ reveals a homogeneous decoration of Zr, which induces a high degree of structural disorder at the GB core, but still remaining partly the crystalline structure of the original GB. The observed segregation layer at the GB was found to be pure Zr with an average solute atomic excess of $2.52\pm0.24\,\frac{at}{nm^2}$ by APT. The structural disorder indicates that in addition to Zr segregation, the grain boundary energy is further reduced by an increase in the GB entropy. This observation supports the two studies

of Khalajhedayati et al. [52] and Pan et al. [66], since also a strong disordering occurs. Furthermore, such a disordering of the GB by Zr will also have a strong effect on the plastic behavior, in particular the dislocation nucleation, as was shown by molecular dynamics simulations [67]. The overall picture on the results can be interpreted as a reduction of the GB free energy by solute segregation and disordering of the atomic structure [3, 2].

2. An asymmetric variant of the $\Sigma 19b\,(2\bar{5}3)$ shows high Zr segregation to GB steps. The steps are incorporated to compensate for the asymmetric inclination of the GB and it was shown that the steps Burgers vector is $[01\bar{1}]$ with pure edge character. Zr was observed to preferentially segregate to these GB steps instead of decorating the planar symmetric GB segments as was found in the pearl structure . Similar to the planar GB, the core structure of the step appears more disordered upon Zr segregation. Such an anomalous segregation behavior was revealed at faceted GBs in silicon and was associated to the core structure and strain of the GB facet junctions [68]. An indication of minor Zr segregation to the symmetric facets is found indirectly by the occurrence of partially disordered structural units. These observations indicate that Zr segregation is strongly affected by GB topology.
3. As shown in fig. 8, minor structural transitions at the symmetric facets are observed. The green sub-unit, or T unit, transforms irregularly to the red, S sub-unit leading to a disruption of the periodicity of the GB structural unit arrangement. This chemically-induced effect is assumed to be related to Zr incorporation in the GB. It implies that different degrees of disordering can be introduced in a GB depending on Zr concentration, as also suggested by atomistic simulations [66]. The SU might transform due to local chemical changes and rearrange in order to minimize the GB free energy.

These atomic scale observations directly confirm the atomistic origins of Zr

segregation to different [111] tilt GBs in Cu. Overall, Zr induces disordering of the structural units as well as the core structure of GB steps, strongly affecting the GB properties. The preferential segregation of Zr to GB steps can have important implications in nc materials since their nanoscale grain size implies a high density of such GB defects [52]. The observations for Zr indicate that it contributes to the microstructure stabilization through the above introduced thermodynamic approach, which is described by a reduced GB energy and thus, a lower driving force for grain growth.

5. Conclusion

In this paper, a systematic study of the atomic scale GB structure and related segregation-induced effects by Ta and Zr on the same GB are investigated. The chosen GBs are two symmetric $\Sigma 19b$ and its slightly asymmetric variants. The employed high resolution microscopy techniques revealed the following conclusions:

1. The two symmetric $\Sigma 19b$ exhibit very complex structures with different structural sub-units and periodicity and cannot be described by the structural unit model. Slightly asymmetric variants of the two GBs reveal a different behavior in compensating the asymmetry. While the $\Sigma 19b, (2\bar{5}3)$ includes steps into the structure, the $\Sigma 19b, (1\bar{8}7)$ includes additional structural sub-units in a periodic manner.
2. Ta segregation was achieved by GB diffusion during an annealing treatment at $600°C$. The formation of nano meter sized Ta precipitates is observed at or close to the GBs. One specific Ta precipitate was found to pin the GB via Zener Pinning by locally distorting the GB plane, which exerts an attractive force on the GB.
3. Zr is found to segregate to the GBs in different ways, depending on the local atomic structure of the GB itself. For an asymmetric variation of the $\Sigma 19b, (1\bar{8}7)$, a homogeneous formation of a pure Zr layer was observed. The presence of the Zr induced a higher disorder in the GB core

and transformed some structural units, by distorting them or removing atomic columns. On an unknown GB with homogeneous Zr segregation, a Zr concentration of $\sim 1.6\,at.\%$ was measured with APT. The asymmetric variation of the $\Sigma 19b, (2\bar{5}3)$, revealed inhomogeneous Zr segregation to its steps, while the symmetric facets are mainly free of Zr. The segregated steps show a much higher disorder compared to the clean steps. Furthermore, small structural transitions of sub-units are observed inhomogeneously along the facets and close to the steps.

4. Interpreting the results with respect to the microstructure stabilization of noncrystalline materials it can be concluded that Ta stabilizes via the kinetic approach. This study visualizes nicely the Zener pinning by Ta particles. The stabilization mechanism of Zr, however, can be explained by the thermodynamic approach. Due to the Zr induced disorder and structural transitions, the GB free energy is lowered. With that the driving force for GB migration is lowered and the microstructure is more stable.

6. Acknowledgment

The authors gratefully thank Dr. Gunther Richter and his team from the Max-Planck-Institut fuer Intelligente Systeme for producing the Cu thin films by molecular beam epitaxy. Furthermore, we acknowledge Tobias Oellers for sputter deposition of Ta and Zr films for our segregation experiments. Finally we thank the European Research Council for funding this project (Grant No: 787446-GB-CORRELATE).

References

[1] A. P. Sutton, V. Vitek, On the structure of tilt grain boundaries in cubic metals I. Symmetrical tilt boundaries, Philosophical Transactions of the Royal Society of London A: Mathematical, Physical and Engineering Sciences 309 (1506) (1983) 1–36.

[2] P. Lejcek, Grain Boundary Segregation in Metals, Vol. 136 of Springer Series in Materials Science, Springer Berlin Heidelberg, Berlin, Heidelberg, 2010.
URL http://link.springer.com/10.1007/978-3-642-12505-8

[3] L. Priester, Grain Boundaries, Vol. 172 of Springer Series in Materials Science, Springer Netherlands, Dordrecht, 2013. doi:10.1007/978-94-007-4969-6.
URL http://link.springer.com/10.1007/978-94-007-4969-6

[4] T. Meiners, Z. Peng, B. Gault, C. H. Liebscher, G. Dehm, Sulfur induced embrittlement in high-purity, polycrystalline copper, Acta Materialia 156 (2018) 64–75. doi:10.1016/j.actamat.2018.06.013.
URL http://www.sciencedirect.com/science/article/pii/S1359645418304816

[5] A. Wimmer, M. Smolka, W. Heinz, T. Detzel, W. Robl, C. Motz, V. Eyert, E. Wimmer, F. Jahnel, R. Treichler, G. Dehm, Temperature dependent transition of intragranular plastic to intergranular brittle failure in electrodeposited Cu micro-tensile samples, Materials Science and Engineering: A 618 (2014) 398–405. doi:10.1016/j.msea.2014.09.029.
URL http://linkinghub.elsevier.com/retrieve/pii/S0921509314011344

[6] H. J. Frost, M. F. Ashby, F. A. Spaepen, A catalogue of [100],[110], and [111] symmetric tilt boundaries in face-centered cubic hard sphere crystals.

[7] Gui Jin Wang, A. P. Sutton, V. Vitek, A computer simulation study of [001] and [111] tilt boundaries: the multiplicity of structures, Acta Metallurgica 32 (7) (1984) 1093–1104. doi:10.1016/0001-6160(84)90013-0.
URL http://www.sciencedirect.com/science/article/pii/0001616084900130

[8] L. S. Shvindlerman, G. Gottstein, V. A. Ivanov, D. A. Molodov, D. Kolesnikov, W. ojkowski, Grain boundary excess free volumedirect

thermodynamic measurement, Journal of Materials Science 41 (23) (2006) 7725–7729. doi:10.1007/s10853-006-0563-0.
URL https://link.springer.com/article/10.1007/s10853-006-0563-0

[9] G. Duscher, M. F. Chisholm, U. Alber, M. Rhle, Bismuth-induced embrittlement of copper grain boundaries, Nature Materials 3 (9) (2004) 621–626. doi:10.1038/nmat1191.
URL http://www.nature.com/doifinder/10.1038/nmat1191

[10] T. Frolov, S. V. Divinski, M. Asta, Y. Mishin, Effect of Interface Phase Transformations on Diffusion and Segregation in High-Angle Grain Boundaries, Physical Review Letters 110 (25). doi:10.1103/PhysRevLett.110.255502.
URL https://link.aps.org/doi/10.1103/PhysRevLett.110.255502

[11] Q. Zhu, A. Samanta, B. Li, R. E. Rudd, T. Frolov, Predicting phase behavior of grain boundaries with evolutionary search and machine learning, Nature Communications 9 (1). doi:10.1038/s41467-018-02937-2.
URL http://www.nature.com/articles/s41467-018-02937-2

[12] Sutton Adrian Peter, Vitek V., Christian John Wyrill, On the structure of tilt grain boundaries in cubic metals II. Asymmetrical tilt boundaries, Philosophical Transactions of the Royal Society of London. Series A, Mathematical and Physical Sciences 309 (1506) (1983) 37–54. doi:10.1098/rsta.1983.0021.
URL https://royalsocietypublishing.org/doi/abs/10.1098/rsta.1983.0021

[13] R. Freitas, R. E. Rudd, M. Asta, T. Frolov, Free energy of grain boundary phases: Atomistic calculations for Σ5(310)[001] grain boundary in Cu, Physical Review Materials 2 (9), arXiv: 1807.03274. doi:10.1103/PhysRevMaterials.2.093603.
URL http://arxiv.org/abs/1807.03274

[14] T. Frolov, M. Asta, Y. Mishin, Phase transformations at interfaces: Observations from atomistic modeling, Current Opinion in Solid State and Materials Science 20 (5) (2016) 308–315. doi:10.1016/j.cossms.2016.05.003.
URL http://www.sciencedirect.com/science/article/pii/S1359028616300304

[15] T. Frolov, D. L. Olmsted, M. Asta, Y. Mishin, Structural phase transformations in metallic grain boundaries, Nature Communications 4 (2013) ncomms2919. doi:10.1038/ncomms2919.
URL https://www.nature.com/articles/ncomms2919

[16] G. H. Bishop, B. Chalmers, A coincidence Edge Dislocation description of grain boundaries, Scripta Metallurgica 2 (2) (1968) 133–139. doi:10.1016/0036-9748(68)90085-9.
URL http://www.sciencedirect.com/science/article/pii/0036974868900859

[17] D. N. Pawaskar, R. Miller, R. Phillips, Structure and energetics of long-period tilt grain boundaries using an effective Hamiltonian, Physical Review B 63 (21) (2001) 214105. doi:10.1103/PhysRevB.63.214105.
URL https://link.aps.org/doi/10.1103/PhysRevB.63.214105

[18] J. D. Rittner, D. N. Seidman, [110] symmetric tilt grain-boundary structures in fcc metals with low stacking-fault energies, Physical Review B 54 (10) (1996) 6999–7015. doi:10.1103/PhysRevB.54.6999.
URL https://link.aps.org/doi/10.1103/PhysRevB.54.6999

[19] J. Han, V. Vitek, D. J. Srolovitz, The grain-boundary structural unit model redux, Acta Materialia 133 (2017) 186–199. doi:10.1016/j.actamat.2017.05.002.
URL http://www.sciencedirect.com/science/article/pii/S1359645417303798

[20] Y. Ikuhara, Grain Boundary and Interface Structures in Ceramics, Journal of the Ceramic Society of Japan 109 (1271) (2001) S110–S120. doi:10.

2109/jcersj.109.1271_S110.
URL https://www.jstage.jst.go.jp/article/jcersj1988/109/1271/109_1271_S110/_article

[21] H. Kurishita, H. Yoshinaga, Y. Ikuhara, Grain Boundary and High-Temperature Strength in SiC, in: S. Smiya, Y. Inomata (Eds.), Silicon Carbide Ceramics1: Fundamental and Solid Reaction, Springer Netherlands, Dordrecht, 1991, pp. 185–211. doi:10.1007/978-94-011-3842-0_9.
URL https://doi.org/10.1007/978-94-011-3842-0_9

[22] A. Stoffers, J. Barthel, C. H. Liebscher, B. Gault, O. Cojocaru-Mirdin, C. Scheu, D. Raabe, Correlating Atom Probe Tomography with Atomic-Resolved Scanning Transmission Electron Microscopy: Example of Segregation at Silicon Grain Boundaries, Microscopy and Microanalysis 23 (02) (2017) 291–299. doi:10.1017/S1431927617000034.
URL https://www.cambridge.org/core/product/identifier/S1431927617000034/type/journal_article

[23] D. Medlin, K. Hattar, J. Zimmerman, F. Abdeljawad, S. Foiles, Defect character at grain boundary facet junctions: Analysis of an asymmetric Sigma 5 grain boundary in Fe, Acta Materialia 124 (2017) 383–396. doi:10.1016/j.actamat.2016.11.017.
URL https://linkinghub.elsevier.com/retrieve/pii/S1359645416308758

[24] N. J. Peter, T. Frolov, M. J. Duarte, R. Hadian, C. Ophus, C. Kirchlechner, C. H. Liebscher, G. Dehm, Segregation-Induced Nanofaceting Transition at an Asymmetric Tilt Grain Boundary in Copper, Physical Review Letters 121 (25). doi:10.1103/PhysRevLett.121.255502.
URL https://link.aps.org/doi/10.1103/PhysRevLett.121.255502

[25] Z. Yu, P. R. Cantwell, Q. Gao, D. Yin, Y. Zhang, N. Zhou, G. S. Rohrer, M. Widom, J. Luo, M. P. Harmer, Segregation-induced ordered superstructures at general grain boundaries in a nickel-bismuth alloy, Science

358 (6359) (2017) 97–101. doi:10.1126/science.aam8256.
URL http://science.sciencemag.org/content/358/6359/97

[26] S. J. Dillon, M. Tang, W. C. Carter, M. P. Harmer, Complexion: A new concept for kinetic engineering in materials science, Acta Materialia 55 (18) (2007) 6208–6218. doi:10.1016/j.actamat.2007.07.029.
URL http://www.sciencedirect.com/science/article/pii/S1359645407004946

[27] A. Kundu, K. Meshinchi Asl, J. Luo, M. P. Harmer, Identification of a bilayer grain boundary complexion in Bi-doped Cu, Scripta Materialia 68 (2013) 146–149. doi:10.1016/j.scriptamat.2012.10.012.

[28] P. R. Cantwell, M. Tang, S. J. Dillon, J. Luo, G. S. Rohrer, M. P. Harmer, Grain boundary complexions, Acta Materialia 62 (Supplement C) (2014) 1–48. doi:10.1016/j.actamat.2013.07.037.
URL http://www.sciencedirect.com/science/article/pii/S1359645413005570

[29] S. J. Dillon, M. P. Harmer, Multiple grain boundary transitions in ceramics: A case study of alumina, Acta Materialia 55 (15) (2007) 5247–5254. doi:10.1016/j.actamat.2007.04.051.
URL http://www.sciencedirect.com/science/article/pii/S1359645407003771

[30] T. Chookajorn, H. A. Murdoch, C. A. Schuh, Design of Stable Nanocrystalline Alloys, Science 337 (6097) (2012) 951–954. doi:10.1126/science.1224737.
URL http://science.sciencemag.org/content/337/6097/951

[31] A. R. Kalidindi, C. A. Schuh, Stability criteria for nanocrystalline alloys, Acta Materialia 132 (2017) 128–137. doi:10.1016/j.actamat.2017.03.029.
URL http://www.sciencedirect.com/science/article/pii/S1359645417302197

[32] K. S. Siow, A. A. O. Tay, P. Oruganti, Mechanical properties of nanocrystalline copper and nickel, Materials Science and Technology 20 (3) (2004) 285–294. doi:10.1179/026708304225010460.
URL http://www.tandfonline.com/doi/full/10.1179/026708304225010460

[33] A. Khalajhedayati, Z. Pan, T. J. Rupert, Manipulating the interfacial structure of nanomaterials to achieve a unique combination of strength and ductility, Nature Communications 7 (2016) 10802. doi:10.1038/ncomms10802.
URL http://www.nature.com/doifinder/10.1038/ncomms10802

[34] A. Khalajhedayati, Z. Pan, T. J. Rupert, Manipulating the interfacial structure of nanomaterials to achieve a unique combination of strength and ductility, Nature Communications 7 (2016) 10802. doi:10.1038/ncomms10802.
URL https://www.nature.com/articles/ncomms10802

[35] C. H. Liebscher, C. Freysoldt, T. Dennenwaldt, T. P. Harzer, G. Dehm, Electronic structure of metastable bcc CuCr alloy thin films: Comparison of electron energy-loss spectroscopy and first-principles calculations, Ultramicroscopydoi:10.1016/j.ultramic.2016.07.011.
URL http://www.sciencedirect.com/science/article/pii/S0304399116301103

[36] J. Schitz, K. W. Jacobsen, A Maximum in the Strength of Nanocrystalline Copper, Science 301 (5638) (2003) 1357–1359. doi:10.1126/science.1086636.
URL http://science.sciencemag.org/content/301/5638/1357

[37] R. Schwaiger, B. Moser, M. Dao, N. Chollacoop, S. Suresh, Some critical experiments on the strain-rate sensitivity of nanocrystalline nickel, Acta Materialia 51 (17) (2003) 5159–5172. doi:10.1016/S1359-6454(03)00365-3.

URL http://www.sciencedirect.com/science/article/pii/S1359645403003653

[38] L. He, E. Ma, Processing and microhardness of bulk Cu-Fe nanocomposites, Nanostructured Materials 7 (3) (1996) 327–339. doi:10.1016/0965-9773(96)00003-7.
URL http://www.sciencedirect.com/science/article/pii/0965977396000037

[39] R. K. Guduru, K. L. Murty, K. M. Youssef, R. O. Scattergood, C. C. Koch, Mechanical behavior of nanocrystalline copper, Materials Science and Engineering: A 463 (1) (2007) 14–21. doi:10.1016/j.msea.2006.07.165.
URL http://www.sciencedirect.com/science/article/pii/S0921509306025548

[40] Y. H. Zhao, Y. T. Zhu, X. Z. Liao, Z. Horita, T. G. Langdon, Tailoring stacking fault energy for high ductility and high strength in ultrafine grained Cu and its alloy, Applied Physics Letters 89 (12) (2006) 121906. doi:10.1063/1.2356310.
URL https://aip.scitation.org/doi/abs/10.1063/1.2356310

[41] E. Nes, N. Ryum, O. Hunderi, On the Zener drag, Acta Metallurgica 33 (1) (1985) 11–22. doi:10.1016/0001-6160(85)90214-7.
URL http://www.sciencedirect.com/science/article/pii/0001616085902147

[42] P. A. Manohar, M. Ferry, T. Chandra, Five Decades of the Zener Equation, ISIJ International 38 (9) (1998) 913–924. doi:10.2355/isijinternational.38.913.
URL https://www.jstage.jst.go.jp/article/isijinternational1989/38/9/38_9_913/_article

[43] K. Darling, B. VanLeeuwen, C. Koch, R. Scattergood, Thermal stability of nanocrystalline FeZr alloys, Materials Science and Engineering: A 527 (15)

(2010) 3572–3580. doi:10.1016/j.msea.2010.02.043.
URL http://linkinghub.elsevier.com/retrieve/pii/S0921509310001930

[44] K. A. Darling, A. J. Roberts, Y. Mishin, S. N. Mathaudhu, L. J. Kecskes, Grain size stabilization of nanocrystalline copper at high temperatures by alloying with tantalum, Journal of Alloys and Compounds 573 (2013) 142–150. doi:10.1016/j.jallcom.2013.03.177.
URL http://www.sciencedirect.com/science/article/pii/S0925838813007081

[45] M. A. Tschopp, H. E. Maupin, US Army Research Laboratory Lightweight and Specialty Metals Branch Research and Development (FY14), Tech. rep., ARMY RESEARCH LAB ABERDEEN PROVING GROUND MD WEAPONS AND MATERIALS RESEARCH DIRECTORATE (2015).

[46] T. Frolov, K. Darling, L. Kecskes, Y. Mishin, Stabilization and strengthening of nanocrystalline copper by alloying with tantalum, Acta Materialia 60 (5) (2012) 2158–2168. doi:10.1016/j.actamat.2012.01.011.
URL http://linkinghub.elsevier.com/retrieve/pii/S1359645412000468

[47] A. I. Zubkov, E. N. Zubarev, O. V. Sobol, M. A. Hlushchenko, E. V. Lutsenko, Structure of vacuum CuTa condensates, Physics of Metals and Metallography 118 (2) (2017) 158–163. doi:10.1134/S0031918X17020156.
URL https://link.springer.com/article/10.1134/S0031918X17020156

[48] H. Wang, M. J. Zaluzec, J. M. Rigsbee, Microstructure and mechanical properties of sputter-deposited Cu 1- x Ta x alloys, Metallurgical and Materials Transactions A 28 (4) (1997) 917–925.

[49] P. R. Subramanian, D. E. Laughlin, The CuTa (Copper-Tantalum) system, Journal of Phase Equilibria 10 (6) (1989) 652–655.

[50] K. A. Darling, M. Rajagopalan, M. Komarasamy, M. A. Bhatia, B. C. Hornbuckle, R. S. Mishra, K. N. Solanki, Extreme creep resistance in a microstructurally stable nanocrystalline alloy, Nature 537 (7620) (2016) 378–381. doi:10.1038/nature19313.
URL https://www.nature.com/articles/nature19313

[51] D. Arias, J. P. Abriata, Cu-Zr (Copper-Zirconium), Journal of Phase Equilibria 11 (5) (1990) 452–459. doi:10.1007/BF02898260.
URL https://doi.org/10.1007/BF02898260

[52] A. Khalajhedayati, Z. Pan, T. J. Rupert, Manipulating the interfacial structure of nanomaterials to achieve a unique combination of strength and ductility, Nature Communications 7 (2016) ncomms10802. doi:10.1038/ncomms10802.
URL https://www.nature.com/articles/ncomms10802

[53] M. A. Atwater, R. O. Scattergood, C. C. Koch, The stabilization of nanocrystalline copper by zirconium, Materials Science and Engineering: A 559 (2013) 250–256. doi:10.1016/j.msea.2012.08.092.
URL http://linkinghub.elsevier.com/retrieve/pii/S0921509312012130

[54] G. Dehm, M. Rhle, G. Ding, R. Raj, Growth and structure of copper thin films deposited on (0001) sapphire by molecular beam epitaxy, Philosophical Magazine Part B 71 (6) (1995) 1111–1124. doi:10.1080/01418639508241899.
URL http://www.tandfonline.com/doi/abs/10.1080/01418639508241899

[55] J. Mayer, L. A. Giannuzzi, T. Kamino, J. Michael, TEM sample preparation and FIB-induced damage, MRS bulletin 32 (5) (2007) 400–407.

[56] C. Li, G. Habler, L. C. Baldwin, R. Abart, An improved FIB sample preparation technique for site-specific plan-view specimens:

A new cutting geometry, Ultramicroscopy 184 (2018) 310–317. doi:10.1016/j.ultramic.2017.09.011.
URL http://www.sciencedirect.com/science/article/pii/S0304399117303522

[57] Urban Knut W., Jia Chun-Lin, Houben Lothar, Lentzen Markus, Mi Shao-Bo, Tillmann Karsten, Negative spherical aberration ultrahigh-resolution imaging in corrected transmission electron microscopy, Philosophical Transactions of the Royal Society A: Mathematical, Physical and Engineering Sciences 367 (1903) (2009) 3735–3753. doi:10.1098/rsta.2009.0134.
URL https://royalsocietypublishing.org/doi/full/10.1098/rsta.2009.0134

[58] B. W. Krakauer, D. N. Seidman, Absolute atomic-scale measurements of the Gibbsian interfacial excess of solute at internal interfaces, Physical Review B 48 (9) (1993) 6724.

[59] P. J. Felfer, C. R. Killmore, J. G. Williams, K. R. Carpenter, S. P. Ringer, J. M. Cairney, A quantitative atom probe study of the Nb excess at prior austenite grain boundaries in a Nb microalloyed strip-cast steel, Acta Materialia 60 (13-14) (2012) 5049–5055. doi:10.1016/j.actamat.2012.06.013.
URL https://linkinghub.elsevier.com/retrieve/pii/S1359645412003758

[60] H. Frost, F. Spaepen, HARD SPHERE MODELS FOR THE STRUCTURE OF GRAIN BOUNDARIES, Journal de Physique Colloques 43 (C6) (1982) C6–73–C6–82. doi:10.1051/jphyscol:1982608.
URL https://hal.archives-ouvertes.fr/jpa-00222288

[61] J. W. Cahn, The impurity-drag effect in grain boundary motion, Acta Metallurgica 10 (9) (1962) 789–798. doi:10.1016/0001-6160(62)90092-5.
URL http://www.sciencedirect.com/science/article/pii/0001616062900925

[62] R. K. Koju, K. A. Darling, L. J. Kecskes, Y. Mishin, Zener Pinning of Grain Boundaries and Structural Stability of Immiscible Alloys, JOM 68 (6) (2016) 1596–1604. doi:10.1007/s11837-016-1899-9.
URL https://doi.org/10.1007/s11837-016-1899-9

[63] R. K. Koju, K. A. Darling, L. J. Kecskes, Y. Mishin, Zener Pinning of Grain Boundaries and Structural Stability of Immiscible Alloys, JOM 68 (6) (2016) 1596–1604. doi:10.1007/s11837-016-1899-9.
URL https://doi.org/10.1007/s11837-016-1899-9

[64] R. K. Koju, K. A. Darling, K. N. Solanki, Y. Mishin, Atomistic modeling of capillary-driven grain boundary motion in Cu-Ta alloys, Acta Materialia 148 (2018) 311–319. doi:10.1016/j.actamat.2018.01.027.
URL http://www.sciencedirect.com/science/article/pii/S1359645418300582

[65] J. D. Schuler, T. J. Rupert, Materials selection rules for amorphous complexion formation in binary metallic alloys, Acta Materialia 140 (2017) 196–205. doi:10.1016/j.actamat.2017.08.042.
URL https://linkinghub.elsevier.com/retrieve/pii/S1359645417306973

[66] Z. Pan, T. J. Rupert, Effect of grain boundary character on segregation-induced structural transitions, Physical Review B 93 (13). doi:10.1103/PhysRevB.93.134113.
URL https://link.aps.org/doi/10.1103/PhysRevB.93.134113

[67] V. Borovikov, M. I. Mendelev, A. H. King, Effects of grain boundary disorder on dislocation emission, Materials Letters 237 (2019) 303–305. doi:10.1016/j.matlet.2018.11.114.
URL http://www.sciencedirect.com/science/article/pii/S0167577X18318810

[68] C. H. Liebscher, A. Stoffers, M. Alam, L. Lymperakis, O. Cojocaru-Mirdin, B. Gault, J. Neugebauer, G. Dehm, C. Scheu, D. Raabe, Strain-Induced

Asymmetric Line Segregation at Faceted Si Grain Boundaries, Physical Review Letters 121 (1). doi:10.1103/PhysRevLett.121.015702.
URL https://link.aps.org/doi/10.1103/PhysRevLett.121.015702

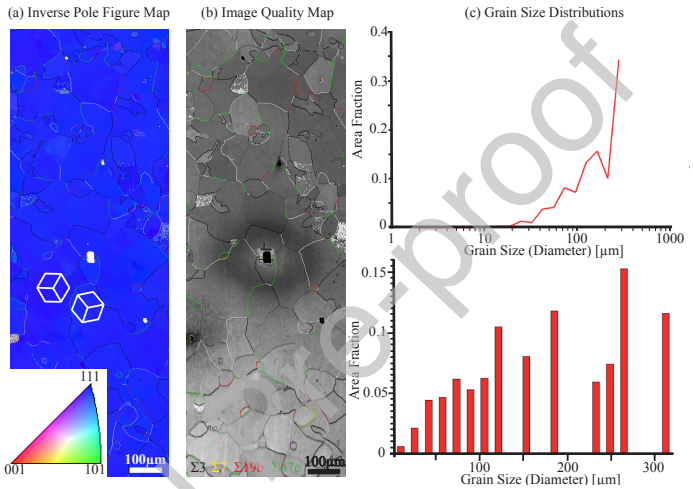

Figure 1: EBSD results of the Cu thin film grown on Sapphire: (a) The inverse pole figure map shows a [111] texture of the Cu film. The colored lines indicate the different GBs species in the film. The two white dices shoe the orientation of the cubic unit cell, further supporting the [111] orientation with different rotations around [111] (b) The image quality map shows the microstructure of the film and also the color coded GBs. The most prominent GBs are low angle GBs (white lines), $\Sigma 3$ twin boundaries (black lines), $\Sigma 7$ GB (yellow lines), $\Sigma 19b$ GBs (red lines) and $\Sigma 37c$ GBs (green lines). (c) These two graphs present two different visualizations of the grain size distribution.

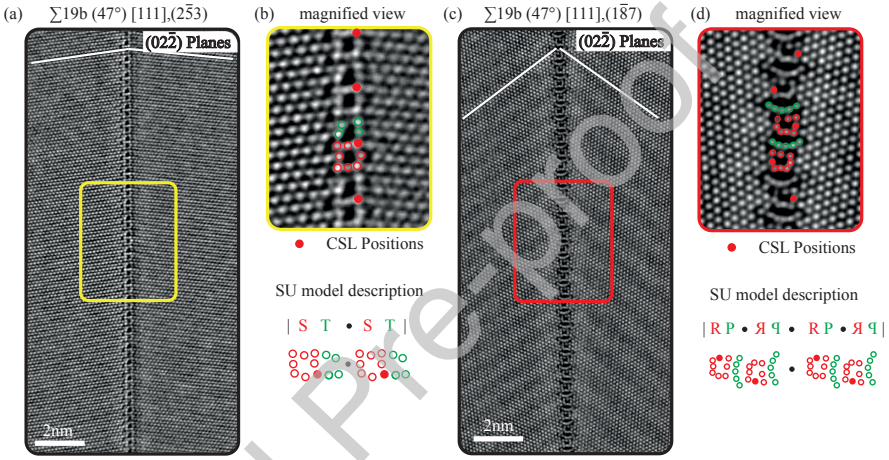

Figure 2: STEM HAADF images of 2 symmetric [111] tilt grain boundaries in plan-view and [111] zone axis orientation. (a) shows the structure of the symmetric $\Sigma\,19b, (2\bar{5}3)$ and (c) symmetric $\Sigma\,19b, (1\bar{8}7)$ GB. The white lines show the $00\bar{2}$ planes and the colored boxes indicate the magnified views on each GB structure, depicted in (b) and (d). The green and red dots represent the structural sub-units and the filled dots represent the coincide side lattice positions. On the bottom of (b) and (d), the respective SU model notation is visualized. meaning of the notation is explained within the text. The STEM images have been smoothed using a Gaussian filter and contrast and brightness were adjusted accordingly.

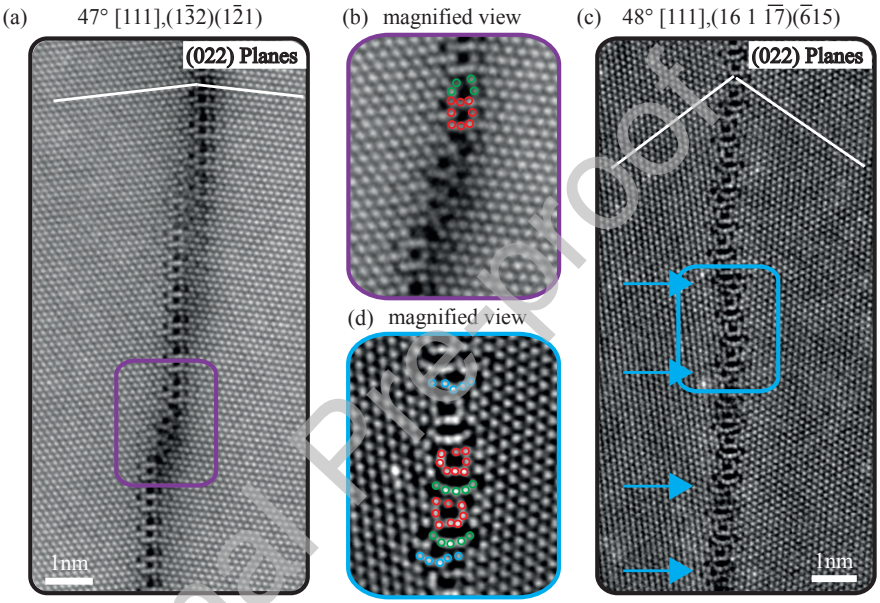

Figure 3: (a) and (c) show asymmetric variations of the GBs shown in Fig. 2 (a) and (c) in plan-view and [111] zone axis orientation. The image depicted in (b), as indicated by a purple box, shows a magnified view on the GB step of (a). In (d), the magnified view in the blue box shows additional structural sub-units of (c), which are also indicated by the blue arrows. The STEM images have been smoothed using a Gaussian filter and contrast and brightness were adjusted accordingly.

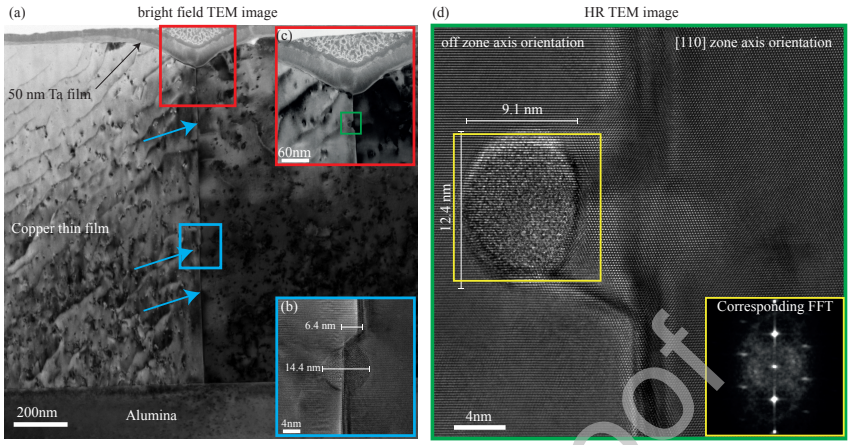

Figure 4: (a) Conventional bright field (BF) image of a cross-section specimen showing the Alumina substrate, the Cu thin film with the GB being perpendicular to the substrate and the Ta thin film. The blue inset (b) shows a spherical particle (HRTEM image) sitting directly on the GB and right in front of a step. The red inset in (c) shows a BF image of another particle sitting next to the GB, which is pinned to the GB. (d) illustrates the atomic structure at that position in a HRTEM micrograph in a [011] zone axis orientation. The yellow rectangle includes the particle and shows the position where the FFT was taken from, which is shown in the lower left corner.

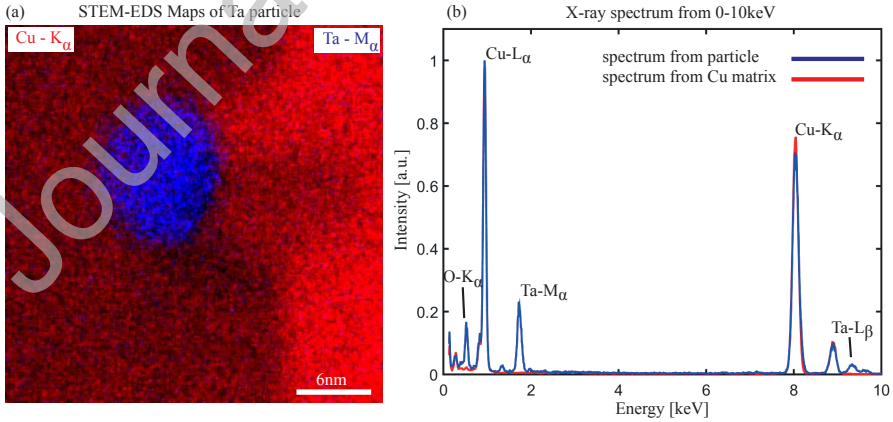

Figure 5: (a) depicts a STEM-EDS maps of the particle using the Cu-K_α (red) and Ta-M_α (blue) edges at the exact position from Fig. 4. In (b) two X-ray spectra are plotted together belonging to the pure Cu grain (red) and to the particle (blue).

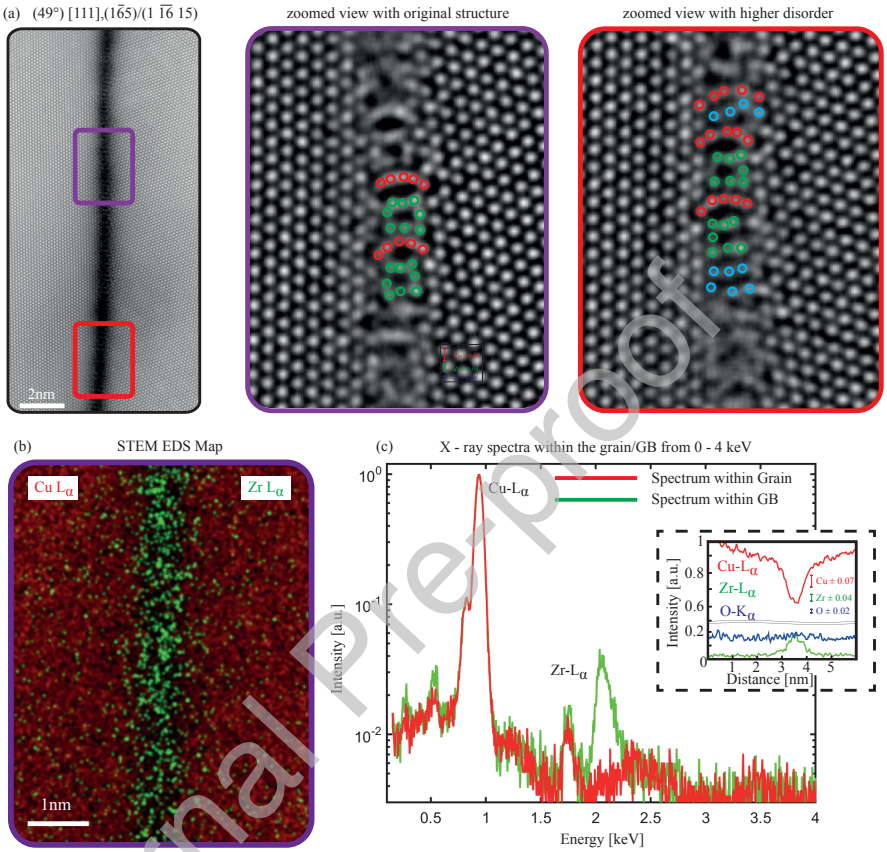

Figure 6: (a) HAADF STEM image in plan-view and [111] zone axis orientation of an asymmetric $\sim 49°$ [111], $(1\bar{6}5)\backslash(1\,\bar{1}\bar{6}\,15)$ GB alloyed with Zr. The image has been smoothed using a Gaussian filter and contrast and brightness were adjusted accordingly. The insets show two different magnified views of the atomic structure using a strong high pass Fourier filter in order to filter out the dark contrast and to highlight the atomic columns. The purple inset shows a region with the original GB structure and the red region with some deviations, as indicated by the colored dots. (b) STEM-EDS measurements, containing a map with the Cu-K_α (red) and Zr-L_α (green). The graph in (b) shows the spectra (in log scale of the y-axis) taken from the grain and the GB, showing an increased Zr concentration at the GB. A concentration profile is depicted in the dashed inset of (c), showing the Cu, Zr and O intensity across the GB. The black square block shows the maximum standard deviation of the corresponding element.

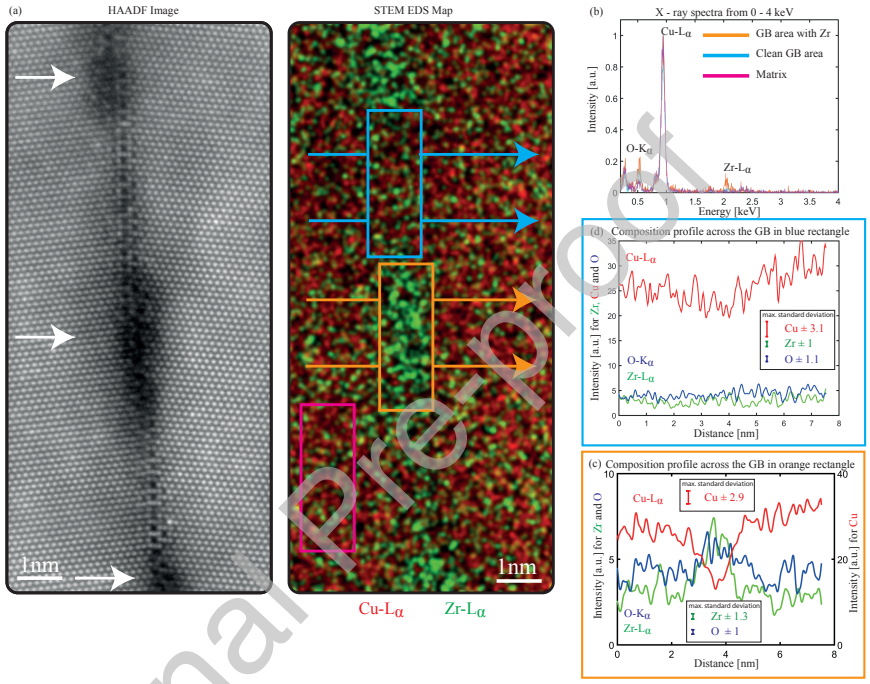

Figure 7: (a) HAADF-STEM micrograph in plan-view and [111] zone axis orientation and STEM-EDS map (Cu-K_α (red) and Zr-L_α (green)) of an asymmetric variant of the zipper structure showing Zr segregation to the GB steps. The colored boxes in the EDS map indicate the positions where the spectra in (b) were taken from. The plot in (b) compares the x-Ray spectra from the GB step, the GB between the steps and the grain. The arrows represent the concentration profiles in (c) and (d) and the black square blocks show the maximum standard deviation of the corresponding element of the line scan. The STEM images have been smoothed using a Gaussian filter and contrast and brightness were adjusted accordingly.

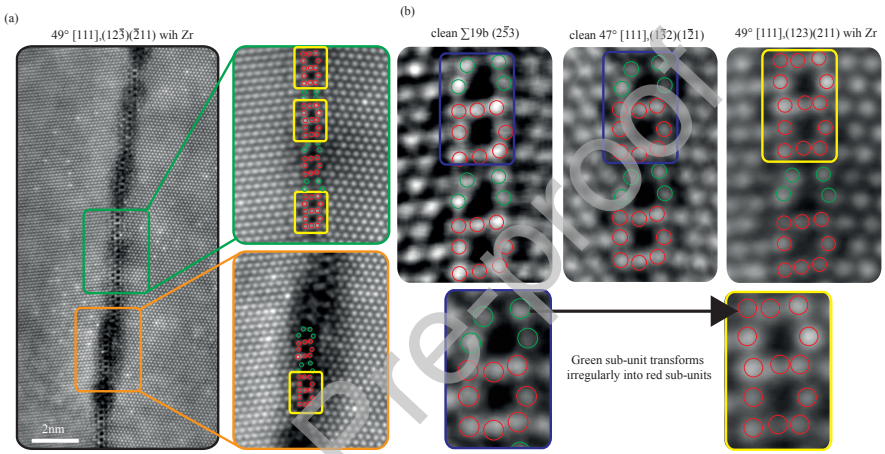

Figure 8: (a) HAADF STEM image in plan-view and [111] zone axis orientation of an asymmetric 49.2° [111], $(12\bar{3})\backslash(\bar{2}11)$ alloyed with Zr, showing dark contrast at all GB steps. The green and orange rectangle show two regions in higher magnification. The green box shows a symmetric facet of the GB. The red and green dots represent the structural sub-unit configuration. In the orange box the disordered structure of a step is shown. (b) HAADF-STEM image of the clean GBs (symmetric and asymmetric) (see also fig. 1). The blue windows marks one structural unit of the GB. Below, the structural units in the yellow, red and blue boxes are compared. The STEM images have been smoothed using a Gaussian filter and contrast and brightness were adjusted accordingly.

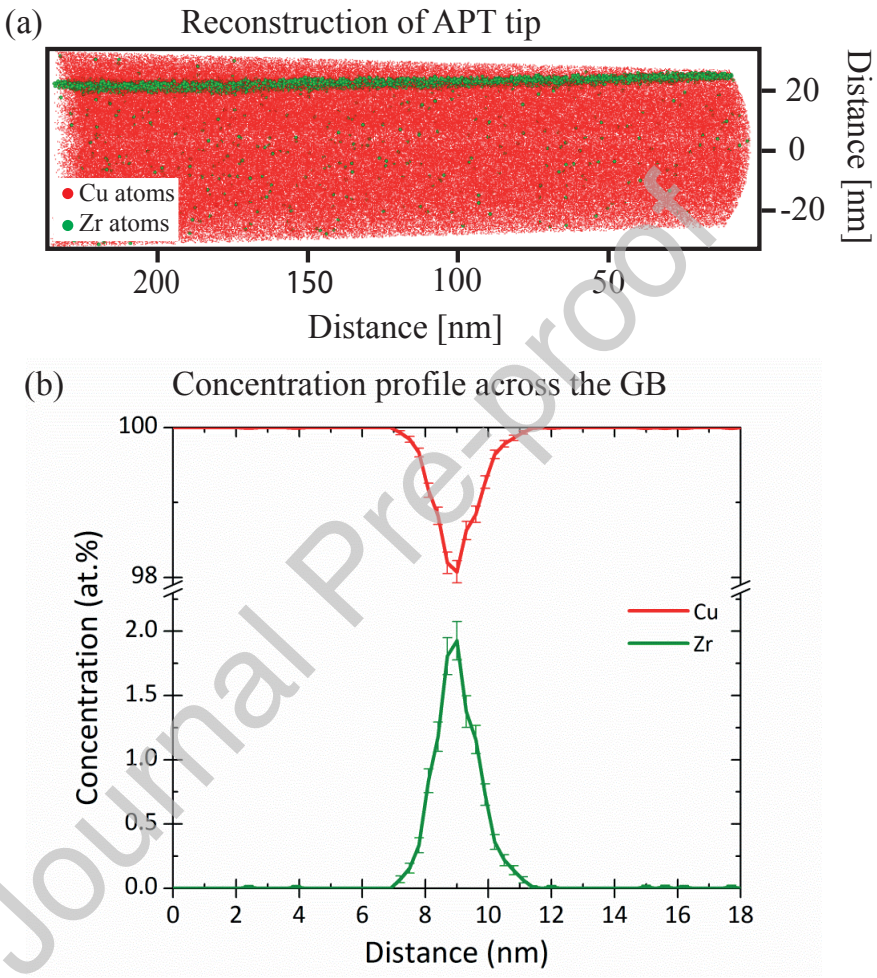

Figure 9: (a) Reconstructed specimen showing Cu atoms in red and Zr atoms in green. A concentration profile of across the GB, showing the concentration of Cu in red and Zr in green, is presented in (c).

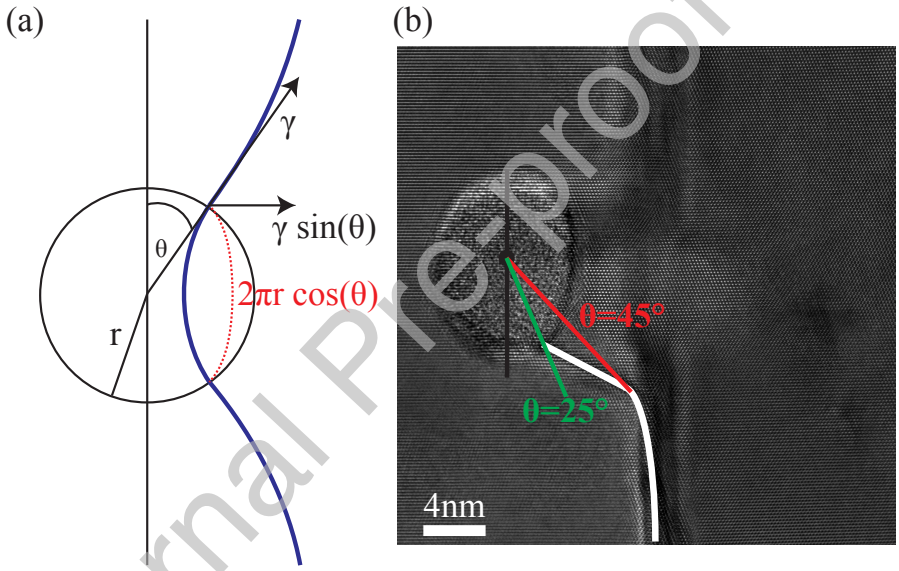

Figure 10: Sketch of the Zener pinning adapted from ref. [42] (a) in comparison with an experimental HRTEM image (b).

Declaration of Interest statements

Manuscript title: Impurity-induced structural transitions at complex [111] tilt grain boundaries in Copper

The authors whose names are listed immediately below certify that they have NO affi liations with or involvement in any organization or entity with any fi nancial interest (such as honoraria; educational grants; participation in speakers' bureaus; membership, employment, consultancies, stock ownership, or other equity interest; and expert testimony or patent-licensing arrangements), or non-fi nancial interest (such as personal or professional relationships, affi liations, knowledge or beliefs) in the subject matter or materials discussed in this manuscript.

The authors whose names are listed immediately below report the following details of affi liation or involvement in an organization or entity with a fi nancial or non-fi nancial interest in the subject matter or materials discussed in this manuscript. Please specify the nature of the confl ict on a separate sheet of paper if the space below is inadequate

Authors: Thorsten Meiners, Gunther Richter, Jazmin M. Duarte, Gerhard Dehm, Christian H. Liebscher